



HAL
open science

The multiwavelength Tully-Fisher relation with spatially resolved HI kinematics

Anastasia A. Ponomareva, Marc A. W. Verheijen, Reynier F. Peletier, Albert Bosma

► **To cite this version:**

Anastasia A. Ponomareva, Marc A. W. Verheijen, Reynier F. Peletier, Albert Bosma. The multiwavelength Tully-Fisher relation with spatially resolved HI kinematics. *Monthly Notices of the Royal Astronomical Society*, 2017, 469 (2), pp.2387-2400. 10.1093/mnras/stx1018 . hal-01678525

HAL Id: hal-01678525

<https://hal.science/hal-01678525v1>

Submitted on 9 May 2018

HAL is a multi-disciplinary open access archive for the deposit and dissemination of scientific research documents, whether they are published or not. The documents may come from teaching and research institutions in France or abroad, or from public or private research centers.

L'archive ouverte pluridisciplinaire **HAL**, est destinée au dépôt et à la diffusion de documents scientifiques de niveau recherche, publiés ou non, émanant des établissements d'enseignement et de recherche français ou étrangers, des laboratoires publics ou privés.

The Multi-Wavelength Tully-Fisher relation with spatially resolved HI kinematics

Anastasia A. Ponomareva^{1,2*}, Marc A. W. Verheijen^{2,3}, Reynier F. Peletier² and Albert Bosma⁴

¹Research School of Astronomy & Astrophysics, Australian National University, Canberra, ACT 2611, Australia

²Kapteyn Astronomical Institute, University of Groningen, Postbus 800, NL-9700 AV Groningen, The Netherlands

³Adjunct Faculty, National Centre for Radio Astrophysics, TIFR, Ganeshkhind, Pune 411007, India

⁴Aix Marseille Univ, CNRS, LAM, Laboratoire d’Astrophysique de Marseille, UMR 7326, F-13388, Marseille, France

12 May 2017

ABSTRACT

In this paper we investigate the statistical properties of the Tully-Fisher relation for a sample of 32 galaxies with measured distances from the Cepheid period–luminosity relation and/or TRGB stars. We take advantage of panchromatic photometry in 12 bands (from FUV to 4.5 μm) and of spatially resolved HI kinematics. We use these data together with three kinematic measures (W_{50}^i , V_{max} and V_{flat}) extracted from the global HI profiles or HI rotation curves, so as to construct 36 correlations allowing us to select the one with the least scatter. We introduce a tightness parameter σ_{\perp} of the TFR, in order to obtain a slope-independent measure of the goodness of fit. We find that the tightest correlation occurs when we select the 3.6 μm photometric band together with the V_{flat} parameter extracted from the HI rotation curve.

Key words: galaxies: fundamental parameters – galaxies: kinematics, dynamics, photometry

1 INTRODUCTION

The Tully-Fisher relation (TFR) is a power-law correlation between the luminosity and the rotation velocity of late-type galaxies (Tully & Fisher 1977). It was empirically established as a powerful tool to measure distances to galaxies independently from their redshift. Knowing only a galaxy’s rotational velocity from the width of its neutral hydrogen (HI) line profile, one can recover the distance modulus to this galaxy by inferring the total intrinsic luminosity from a calibrator sample. Thus, to obtain accurate distances, a number of studies of the statistical properties of the TFR were done in the past, aiming to reduce as much as possible the observed scatter in the relation, e.g. the Cosmic Flows programme (Courtois et al. 2011; Courtois & Tully 2012; Tully & Courtois 2012).

Understanding the origin of the TFR is one of the main challenges for theories of galaxy formation and evolution. From a theoretical point of view, a perfect correlation between the intrinsic luminosity and rotational velocity of a galaxy is currently explained as a relation between the hosting dark matter halo and its baryonic content, assuming a

direct link between luminosity and baryonic mass. The detailed statistical properties of the TFR provide important constraints to semi-analytical models and numerical simulations of galaxy formation (Navarro & Steinmetz 2000; Vogelsberger et al. 2014; Schaye et al. 2015; Macciò et al. 2016). It is thus an important test for any theory of galaxy formation and evolution to reproduce the slope, scatter and the zero point of the TFR in different photometric bands simultaneously. The TFR can also constrain theories about the distribution of mass within galaxies, e.g. it was shown by Courteau et al. (2003) that barred and unbarred galaxies follow the same TFR, even though barred galaxies could be less dark matter dominated within their optical radius (Weiner et al. 2001).

Over the past decades, the scatter in the observed TFR has been decreased significantly by more accurate photometric measures. As first suggested by Aaronson et al. (1979), the TFR can be tightened by moving from optical to NIR bands, where the old stars peak in luminosity and provide a good proxy for the stellar mass of the galaxies (Peletier & Willner 1991). The advent of infra-red arrays shifted photometry to the JHK bands and then to space-based infrared photometry, e.g. with the *Spitzer Space Telescope* (Werner et al. 2004). However, despite the obvious advantages of deep

* E-mail: ponomareva@astro.rug.nl

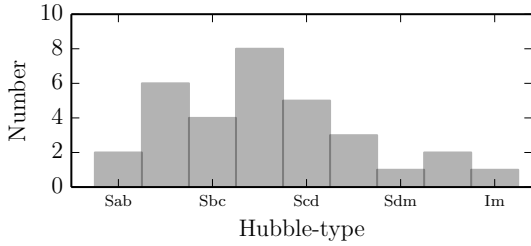


Figure 1. The distribution of morphological types of the galaxies in our sample.

near-infrared luminosities, it is still not clear at which NIR wavelengths the smallest scatter in the TFr can be achieved. For example, [Bernstein et al. \(1994\)](#), using 23 spirals in the Coma cluster found that the H-band TFr does not have less scatter than the I-band relation. [Sorce et al. \(2013\)](#) claim that the $3.6 \mu\text{m}$ TFr has even larger scatter than the I-band TFr ([Tully & Courtois 2012](#), hereafter [TC12](#)). In fact, accurate infrared photometry led to the point where the measurement errors on the total luminosity can no longer explain the observed scatter.

Yet, so far, very little attention has been given to improving the measurements of the rotation velocity which is, as mentioned before, thought to be strongly related dynamically to the dark matter halo. Notably, the width and shape of the global HI profile are determined by the detailed distribution of the HI gas in the disk, the shape of a galaxy’s rotation curve, and the presence of non-circular motions and/or a warp. It is impossible to take into account all these important aspects while inferring the rotational velocity of a galaxy from the integrated global HI profile. This notion has motivated observational studies which took advantage of optical rotation curves, using $H\alpha$ long slit spectroscopy ([Rubin et al. 1980, 1985](#); [Pizagno et al. 2007](#)). However, the rotational velocity at the optical radius does not probe the dark matter halo potential properly, since the data do not extend far enough in radius. Of course, for an axisymmetric galaxy with a monotonically rising rotation curve that reaches a constant flat part in a non-warped outer gas disk, the rotational velocity is reasonably well-defined and can be estimated from the corrected width of the global HI profile. Unfortunately, galaxies often are not that well-behaved and the column–density distribution and kinematic structure of their gas disks may significantly affect the shape and width of the global HI profiles, introducing errors on the derived rotational velocity that can not be corrected for without further information.

Detailed studies of galaxy rotation curves using 21-cm aperture synthesis imaging ([Bosma 1981](#); [van Albada et al. 1985](#); [Begeman 1989](#); [Broeils & van Woerden 1994](#); [Verheijen 2001](#); [Swaters et al. 2002](#); [Noordermeer 2006](#); [de Blok et al. 2014](#)), show that the shape of the rotation curve strongly depends on the morphology and surface brightness of the galaxy, introducing deviations from the classical flat rotation curve. For instance, it is well-known that late type dwarf galaxies have slowly rising rotation curves. In this case the observed maximal rotational velocity (V_{max}) will underestimate the velocity of the halo, simply because the rotation curve is not reaching the flat part (V_{flat}). The other extreme

Name	Hubble type	P.A. deg.	Incl. deg.	Distance Mpc
NGC 0055	SB(s)m	110±3	78±7	1.98±0.05
NGC 0224	SA(s)b	37±1	78±1	0.76±0.02
NGC 0247	SAB(s)d	169±3	77±2	3.51±0.09
NGC 0253	SAB(s)c	230±2	77±1	3.56±0.13
NGC 0300	SA(s)d	290±3	46±6	1.97±0.05
NGC 0925	SAB(s)d	283±2	61±5	8.91±0.28
NGC 1365	SB(s)b	218±2	39±8	17.7±0.81
NGC 2366	IB(s)m	42±6	68±5	3.34±0.09
NGC 2403	SAB(s)cd	124±1	61±3	3.17±0.08
NGC 2541	SA(s)cd	170±3	64±4	11.5±0.47
NGC 2841	SA(r)b	150±3	70±2	14.5±0.47
NGC 2976	SAC pec	323±1	61±5	3.63±0.13
NGC 3031	SA(s)ab	330±4	59±5	3.61±0.09
NGC 3109	SB(s)m	92±3	80±4	1.37±0.03
NGC 3198	SB(rs)c	215±5	70±1	13.3±0.55
IC 2574	SAB(s)m	55±5	65±10	3.89±0.14
NGC 3319	SB(rs)cd	33±2	57±4	13.0±0.53
NGC 3351	SB(r)b	192±1	47±5	10.4±0.28
NGC 3370	SA(s)c	327±3	55±5	26.1±0.72
NGC 3621	SA(s)d	344±4	65±7	6.72±0.18
NGC 3627	SAB(s)b	172±1	58±5	9.03±0.29
NGC 4244	SA(s)cd	222±1	88±3	4.61±0.19
NGC 4258	SAB(s)bc	331±1	72±3	7.31±0.16
NGC 4414	SA(rs)c?	160±2	52±4	17.8±0.74
NGC 4535	SAB(s)c	180±1	41±5	16.1±0.66
NGC 4536	SAB(rs)bc	300±3	69±4	14.6±0.60
NGC 4605	SB(s)c pec	293±2	69±5	5.54±0.25
NGC 4639	SAB(rs)bc	311±1	42±2	22.0±0.71
NGC 4725	SAB(r)ab pec	30±3	50±5	12.5±0.46
NGC 5584	SAB(rs)cd	152±4	44±4	22.4±0.72
NGC 7331	SA(s)b	169±3	75±3	13.8±0.51
NGC 7793	SA(s)d	290±2	50±3	3.58±0.11

Table 1. The Tully-Fisher Calibrator Sample. Column (1): galaxy name (as shown in [NED](#)); Column (2): Hubble type (as shown in [NED](#)); Column (3): kinematic position angle (Paper I); Column (4): kinematic inclination (Paper I); Column (5): Distance in Mpc provided by The Extragalactic Distance Database ([EDD](#)), [Tully et al. 2009](#).

case are massive early-type spirals, which usually show a fast rise of the rotation curve until the maximum velocity (V_{max}) is reached, usually within the optical disk, beyond which the rotation curve significantly declines, reaching the flat part with much lower velocity ([Bosma 1981](#); [Casertano & van Gorkom 1991](#); [Verheijen 2001](#); [Noordermeer 2006](#)). In this case, the mass of the halo, if derived using V_{max} , will be overestimated for the most massive galaxies, which can cause a curvature in the TFr ([Neill et al. 2014](#)). It was shown by [Verheijen \(2001\)](#) with a study of spiral galaxies in the Ursa Major cluster, that the statistical properties of the TFr depend on the shape of the rotation curves, and that the observed scatter is reduced significantly when extended HI rotation curves are available to substitute the corrected width of the global HI profile with V_{flat} from the rotation curve as a kinematic measure.

It is very important to realise that the literature contains many observational results on the TFr which are often inconsistent with each other. This is largely due to different corrections applied to the observables, e.g. for extinction or inclination, due to different photometric systems, due to different observing techniques or due to different samples. This makes it very complicated to compare the various studies in

a simple manner. In this paper we establish TFRs based on a homogeneous analysis of imaging data obtained in 12 photometric bands from UV to IR (the detailed photometric analysis will be presented in a companion paper), while taking advantage of spatially resolved HI kinematics as reported in Ponomareva et al. (2016), hereafter Paper I. We study the statistical properties of the TFR to investigate the link between the host dark matter DM halo and the various stellar populations of galaxies, which peak in different bands. Such a homogeneous analysis allows us to obtain a better understanding of the physical phenomenon of the TFR, especially as a tool to study the internal structure of galaxies.

This paper is organised as follows: Section 2 describes the sample of calibrator galaxies. Section 3 describes the collected photometric data. Section 4 describes the HI data. Section 5 summarises the corrections which were applied to the observables. Section 6 discusses the statistical properties of the constructed TFRs. Section 7 presents the summary and concluding remarks.

2 THE SAMPLE

In our study we are interested in the slope and intrinsic tightness of the TFR. We are not aiming to maximise the number of galaxies in the sample, but rather to increase the quality of the kinematic measures for a representative sample of galaxies with independent distance measurements. Thus, we analysed aperture synthesis imaging HI data to derive high-quality rotation curves (Paper I). The independent distances to our galaxies were measured from the Cepheid period–luminosity relation (Freedman et al. 2001) or/and from the tip of the red giant branch (Rizzi et al. 2007) and are provided by The Extragalactic Distance Database (EDD) (Tully et al. 2009). Independently measured distances reduce the error in the absolute magnitude of a galaxy and therefore reduce the impact of distance uncertainties on the observed scatter of the TFR. For example, in our case, distance uncertainties contribute only $\sigma_{dist} = 0.07$ mag to the total observed scatter of the TFR, which is much lower in comparison with $\sigma_{dist} = 0.41$ mag if the Hubble–flow distances are adopted. We adopt a sample of 32 large, relatively nearby galaxies from the zero point (ZP) calibrator sample described in TC12. Their selection criteria for galaxies included in the sample completely satisfy our requirements: 1) morphological types Sab and later (Figure 1), 2) inclinations no less than 45° , 3) HI profiles with adequate S/N, 4) global HI profiles without evidence of distortion or blending. Their selection criteria give us confidence that the adopted galaxies are kinematically well-behaved with regularly rotating, extended HI disks. In Paper I it was found that this confidence was largely justified, but that the corrected width of the global HI profile is not always an accurate representation of V_{flat} . Global parameters of the sample galaxies are summarised in Table 1.

3 PHOTOMETRIC DATA

To study the wavelength dependence of the statistical properties of the TFR requires not only a representative sample, but a systematic, homogeneous approach in deriving the

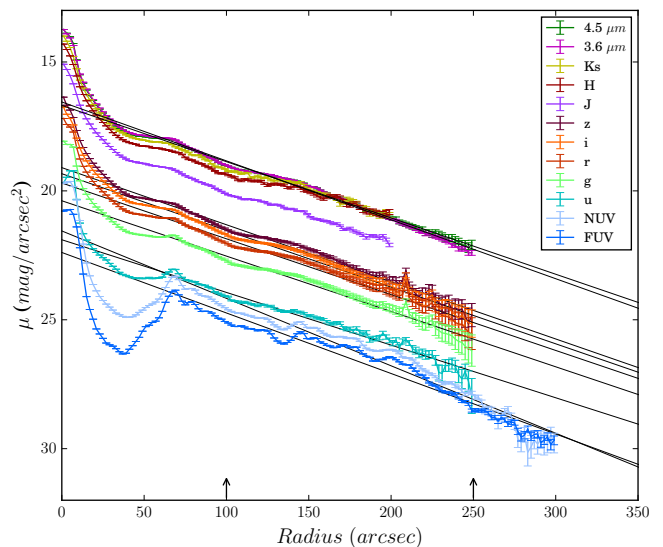


Figure 2. Surface brightness profiles of NGC 3351 for 12 photometric bands. The region within which the exponential disk fit was done is indicated with arrows. Black lines show the exponential disk fit to the profile. Profiles are terminated at their R_{lim} .

main photometric properties of galaxies. We use 12 bands per galaxy (FUV , NUV , u , g , r , i , z , J , H , K_s , 3.6 , $4.5 \mu m$) for 21 galaxies, and 7 bands for the remaining 11 galaxies in our sample due to the absence of SDSS imaging data. This broad wavelength coverage allows us to measure the relative luminosity of old and young stars within a galaxy and to perform SED fits in a forthcoming paper to estimate their stellar masses.

The FUV and NUV images were collected from the various Galaxy Evolution Explorer (GALEX, Martin et al. 2005) space telescope data archives. Since young, stars which peak in UV, have a very low contribution to the total mass of a galaxy, a very large scatter in the UV–based TFRs might be expected. Nevertheless, we consider these bands in our study as well.

To obtain optical photometry, we use the SDSS Data Release 9 (DR9, Ahn et al. 2012), but note that SDSS photometry is only available for 21 galaxies in our sample. Therefore we consider TFRs in the SDSS bands for a smaller number of galaxies. However, we point out that the SDSS–subsample still spans a wide luminosity range.

We collected a wide range of NIR images: J , H , K_s bands from the Two-Micron All Sky Survey (2MASS, Skrutskie et al. 2006) and $3.6 \mu m$ and $4.5 \mu m$ from the Spitzer Survey for Stellar Structure in Galaxies (S^4G , Sheth et al. 2010). All data were gathered from the IRSA archive.

3.1 Total Magnitudes

All data were homogeneously analysed and the total magnitudes were derived for every galaxy in each band.

First, the aperture magnitudes (m_{ap}) were calculated by integrating the surface brightness profile (SBP) in each band within a fixed radius (R_{lim}). R_{lim} was chosen after a visual inspection of every profile, as the largest radius at

which the surface brightness (μ_{lim}) is still reliable. Given the varying quality of the data, R_{lim} may differ for various bands. In Figure 2 the SBPs are shown for NGC 3351 in all bands within their R_{lim} .

Then, linear fits were made to the outer part of each SBP (except for the 2MASS data¹), which characterises the exponential drop of surface brightness of a galaxy due to the disk component. The radial range within which the fit was made was identified through visual inspection and is shown in Figure 2 with vertical arrows. This procedure is in essence the “mark the disk” procedure described by de Jong (1996). We assume that beyond R_{lim} the SBP continues to drop exponentially without any truncations and/or breaks. Under this assumption Tully et al. (1996) showed that the extended magnitude does not depend on the scale length of the disk or on the ellipticity of the galaxy, but only on the number Δn of disk scale lengths within R_{lim} . Hence it can be calculated as :

$$\Delta m_{ext} = 2.5 \log[1 - (1 + \Delta n)e^{-\Delta n}], \quad (1)$$

with

$$\Delta n = (\mu_{lim} - \mu_0)/1.086. \quad (2)$$

Then, the total magnitudes follow from $m_{tot} = m_{ap} + m_{ext}$.

Note that the detailed photometric analysis and final data products will be presented in a companion paper.

4 HI DATA

We are interested in studying the statistical properties of the TFR at various wavelengths based on rotational velocities derived from global HI profiles and high-quality rotation curves. The ideal data for this work are HI radio aperture synthesis imaging data which provide the global HI profiles, as well as the spatially resolved rotation curves.

We collected the HI radio synthesis-imaging data for 29 galaxies from the literature. Most of these galaxies were observed previously as part of larger HI surveys (THINGS, WHISP, HALOGAS, etc). We observed the remaining three galaxies with the Giant Radio Metrewave Telescope (GMRT) in March 2014. All data cubes were analysed homogeneously and the following data products were delivered for all 32 galaxies in our sample: global HI profiles, integrated HI column-density maps, HI surface-density profiles and high-quality rotation curves derived from highly-resolved, two-dimensional velocity fields.

These data products, along with a detailed description of the observations, data reduction and analyses, are presented in Paper I. Here, we summarize the relevant kinematic information, obtained from these HI data.

¹ 2MASS survey images are too shallow and the SBPs do not extend enough to apply the method of recovering the total light as described above. Therefore, for J, H, K and $3.6 \mu m$ bands we constructed the growth curves and measured the colours $J - [3.6]$, $H - [3.6]$ and $K - [3.6]$ at the last reliable measured point of the growth curves of the 2MASS bands within the same radius. We fixed these colours and calculated 2MASS total magnitudes as $M_{tot}^{JHK} = M_{tot}^{[3.6]} + (JHK_{R_{limp}} - [3.6]_{R_{limp}})$, where R_{limp} is the radius at which the last measure point of the 2MASS band was measured.

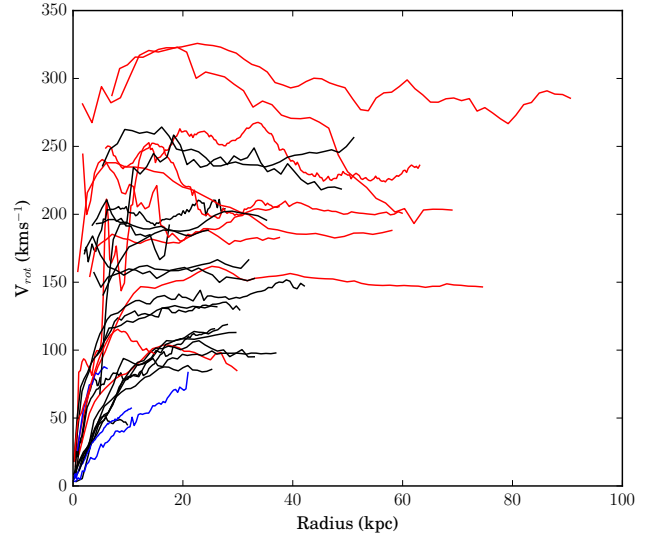


Figure 3. Compilation of extended HI rotation curves of our sample galaxies plotted on the same linear scale. Blue curves belong to galaxies with Rrc ($V_{max} < V_{flat}$) and red curves are declining rotation curves ($V_{max} > V_{flat}$).

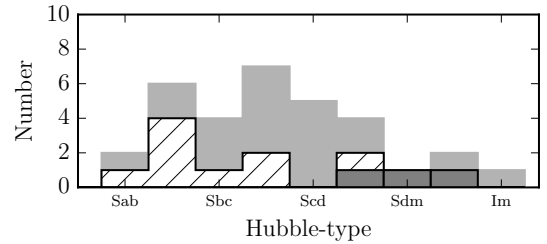


Figure 4. Rotation curves morphology distribution within the sample. The light hatched region shows galaxies with declining rotation curves. The dark shaded area corresponds to galaxies with rising rotation curves.

4.1 Rotational velocities

There are several methods to measure the rotational velocities of spiral galaxies using HI data. First, from the width of the HI 21cm line profile, where the corrected width of the profile relates to the rotational velocity as $W^i = 2V_{rot}$. Second, from the spatially resolved HI velocity fields which allow the derivation of the high-quality rotation curves. While the former is much faster to obtain observationally with single-dish telescopes and can therefore be used for a large number of galaxies, the latter provides valuable extra information.

Amongst others, Verheijen (2001) showed that rotation curves of spiral galaxies have different shapes, which mostly depend on the morphological type and luminosity of a galaxy. The advantage of our sample is that it covers all types of rotation curves: rising (Rrc) for dwarf galaxies ($V_{max} < V_{flat}$), classical flat (Frc) for the intermediate types ($V_{max} = V_{flat}$), and declining (Drc) for the early-type spirals ($V_{max} > V_{flat}$). The “family” of rotation curves of our sample is shown in Figure 3. Moreover, Figure 4 demonstrates that declining rotation curves tend to belong mainly

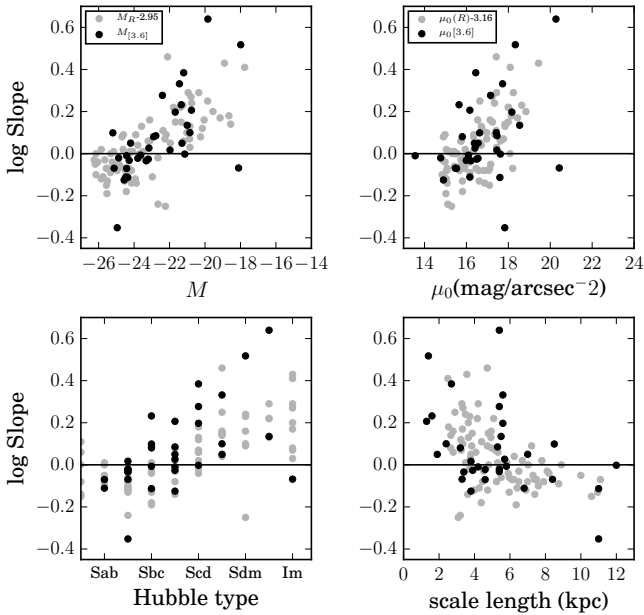


Figure 5. Slopes of the outer part of rotation curves and their correlation with galaxy parameters. Our sample is shown with black dots. Absolute magnitude and disk central surface brightness are measured in the $3.6 \mu\text{m}$ band. A compilation of various observational samples (Casertano & van Gorkom 1991; Verheijen & Sancisi 2001; Spekkens & Giovanelli 2006; Noordermeer et al. 2007; Swaters et al. 2009) is shown with grey symbols. For the reference samples, the absolute magnitude and disk central surface brightness are measured in the R band and then matched to our sample using the colour term $(R - [3.6]) = 2.95$ and $\mu_0(R) - \mu_0[3.6] = 3.16$.

to massive early-type spirals, while rising rotation curves are common for late type galaxies (Casertano & van Gorkom 1991; Verheijen 2001; Noordermeer et al. 2007; Oh et al. 2008; Swaters et al. 2009; de Blok et al. 2014).

To quantitatively describe the shape of a rotation curve, we measure the slope of the outer part of a rotation curve between the radius at 2.2 disk scale lengths, measured from the $3.6 \mu\text{m}$ surface brightness profile (SBP), and the outermost point:

$$S_{2.2h, lmp} = \frac{\text{Log}(V_{2.2h}/V_{lmp})}{\text{Log}(R_{2.2h}/R_{lmp})} \quad (3)$$

where $V_{2.2h}$ and V_{lmp} are the rotational velocities at the radius equal to $2.2h$ ($R_{2.2h}$) and at the radius of the last measured point (R_{lmp}). Thus, a slope equal to zero belongs to a flat rotation curve, a positive slope to a rising rotation curve and a negative slope to a declining rotation curve. Figure 5 demonstrates $S_{2.2h, lmp}$ as a function of global galactic properties. There are prominent correlations with Hubble type, as was suggested earlier (Figure 4), and with the absolute magnitude. In grey we show a compilation of various samples from previous studies (Casertano & van Gorkom 1991; Verheijen & Sancisi 2001; Spekkens & Giovanelli 2006; Noordermeer et al. 2007; Swaters et al. 2009), to point out that our sample is not in any way peculiar and follows the same trends found in previous studies.

The shape of the global HI profile may hint at the shape

Name	V_{sys} km s^{-1}	W_{50}^i km s^{-1}	V_{max} km s^{-1}	V_{flat} km s^{-1}	Slope
NGC 0055	130 ± 5	185 ± 4	85 ± 1	85 ± 2	0.135
NGC 0224	-300 ± 3	517 ± 5	261 ± 2	230 ± 7	-0.02
NGC 0247	160 ± 10	200 ± 3	110 ± 5	110 ± 5	0.332
NGC 0253	240 ± 5	410 ± 3	200 ± 4	200 ± 4	-0.01
NGC 0300	135 ± 10	160 ± 5	103 ± 3	85 ± 7	0.100
NGC 0925	550 ± 5	200 ± 8	115 ± 4	115 ± 4	0.277
NGC 1365	1640 ± 3	380 ± 10	322 ± 6	215 ± 4	-0.352
NGC 2366	107 ± 10	100 ± 10	45 ± 5	45 ± 5	-0.068
NGC 2403	135 ± 1	225 ± 1	128 ± 1	128 ± 1	0.017
NGC 2541	560 ± 5	200 ± 6	100 ± 4	100 ± 4	0.384
NGC 2841	640 ± 20	590 ± 3	325 ± 2	290 ± 6	-0.069
NGC 2976	5 ± 5	130 ± 7	78 ± 4	78 ± 4	0.206
NGC 3031	-40 ± 10	415 ± 6	249 ± 3	215 ± 9	-0.070
NGC 3109	404 ± 5	110 ± 1	57 ± 2	–	0.517
NGC 3198	660 ± 10	315 ± 4	161 ± 2	154 ± 4	0.026
IC 2574	51 ± 3	105 ± 2	75 ± 5	–	0.639
NGC 3319	730 ± 4	195 ± 6	112 ± 10	112 ± 10	0.197
NGC 3351	780 ± 5	260 ± 6	190 ± 5	176 ± 8	-0.022
NGC 3370	1280 ± 15	275 ± 4	152 ± 4	152 ± 4	-0.026
NGC 3621	730 ± 13	275 ± 7	145 ± 5	145 ± 5	0.080
NGC 3627	715 ± 10	340 ± 7	183 ± 7	183 ± 7	-0.032
NGC 4244	245 ± 3	195 ± 6	110 ± 6	110 ± 6	-0.002
NGC 4258	445 ± 15	420 ± 6	242 ± 5	200 ± 5	-0.113
NGC 4414	715 ± 7	375 ± 6	237 ± 10	185 ± 10	-0.125
NGC 4535	1965 ± 5	270 ± 6	195 ± 4	195 ± 4	0.050
NGC 4536	1800 ± 6	320 ± 6	161 ± 10	161 ± 10	-0.007
NGC 4605	160 ± 15	150 ± 15	87 ± 4	–	0.232
NGC 4639	978 ± 20	275 ± 6	188 ± 1	188 ± 1	-0.034
NGC 4725	1220 ± 14	400 ± 4	215 ± 5	215 ± 5	-0.111
NGC 5584	1640 ± 6	190 ± 10	132 ± 2	132 ± 2	0.085
NGC 7331	815 ± 5	500 ± 10	275 ± 5	275 ± 5	0.098
NGC 7793	228 ± 70	174 ± 10	118 ± 8	95 ± 8	0.049

Table 2. Results from the HI kinematics analysis. Column (1): galaxy name; Column (2): systemic velocity; Column (3): width of the global HI profile at 50% level; Column (4): maximal rotational velocity; Column (5): rotational velocity of the flat part of rotation curve. Column (6): slope of the outer part of the rotation curve.

of the rotation curve in several cases. First, a boxy or Gaussian shape profile is an indication for a rising rotation curve for which the velocity of the dark matter halo is underestimated from the profile width. In these profiles, the classical double peak is missing because the constant, flat part of the rotation curve is not sampled by an extended HI disk. In its turn, the classical double peak profile gives an indication that the rotation curve of a galaxy will reach its flat part. Figure 6 demonstrates the difference in the velocity obtained using W_{50}^i (corrected for inclination), compared to V_{max} (upper panel) and V_{flat} (bottom panel) as derived from the rotation curves. It is clear that the main outliers are the galaxies with either rising (blue) or declining (red) rotation curves. Thus, the rotational velocity measured from W_{50}^i will be underestimated in comparison with V_{max} , and overestimated in comparison with V_{flat} . Therefore, one should take into account that the rotational velocity derived from the width of the global profile may differ from the velocity measured from the spatially resolved rotation curve.

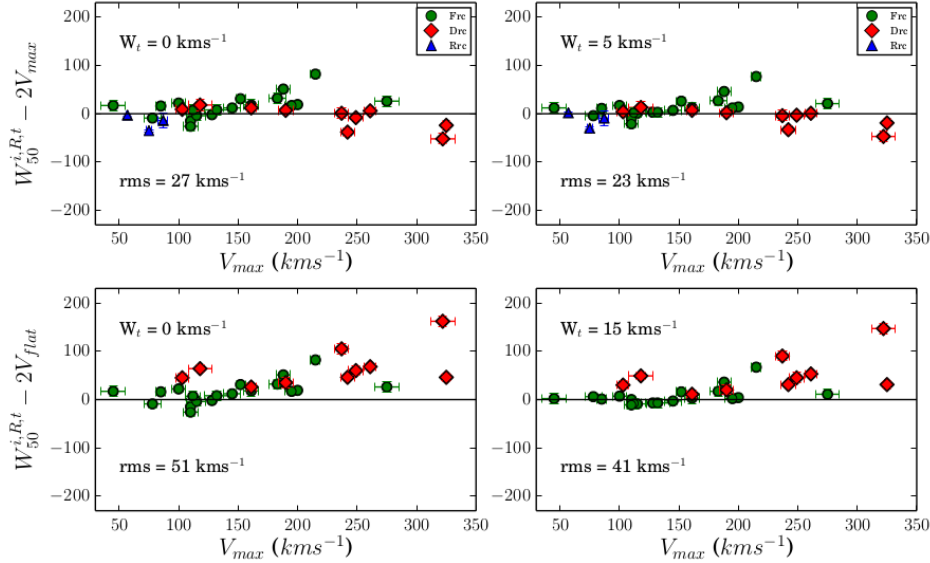


Figure 6. Comparison of the global profile widths at the 50% level, corrected for inclination, instrumental broadening and random motions $W_{50}^{i,R,t}$ with $2V_{max}$ (upper panels) and $2V_{flat}$ (bottom panels). Blue symbols indicate galaxies with Rrc ($V_{max} < V_{flat}$) and red symbols indicate galaxies with declining rotation curves ($V_{max} > V_{flat}$). Green symbols show flat rotation curves ($V_{max} = V_{flat}$).

5 CORRECTIONS TO OBSERVABLES

5.1 Photometry

As a photometric measure for the TFR we use the corrected absolute total magnitudes $M_T^{b,i}(\lambda)$:

$$M_T^{b,i}(\lambda) = m_T(\lambda) - A_\lambda^i - A_\lambda^b - DM, \quad (4)$$

where $m_T(\lambda)$ is the apparent total magnitude (Section 3.1), A_λ^i is the internal extinction correction, A_λ^b is the Galactic extinction correction and DM is the distance modulus, based on the distance given in Table 1. It is important to note, that we not only measure the total magnitudes for all galaxies in each band in the same manner, we also use the same methods to apply corrections due to the Galactic and internal extinction, therefore we can perform a fair comparisons between the TFRs in various bands. The detailed analysis of the photometrical corrections can be found in a forthcoming companion paper.

5.2 HI kinematics

In this section we summarize the main corrections that were applied to the kinematic measures.

The global HI linewidths were corrected for:

(i) Instrumental broadening, which depends on the instrumental velocity resolution and on the steepness of the wings of the velocity profile, following [Verheijen & Sancisi \(2001\)](#).

(ii) Turbulent motions, which depend on the level at which the width of the profile was measured (20% or 50% of the peak flux, [Verheijen & Sancisi 2001](#)). Figure 6 demonstrates the difference between the corrected (right panels) and non-corrected (left panels) widths of the integrated HI profile and the velocity derived from the rotation curve.

(iii) Inclination, according to the formula $W_{50,20}^i =$

$W_{50,20}/\sin(i_{kin})$, where i_{kin} is the kinematic inclination angle derived from the HI velocity fields ([Paper I](#)), in order to represent the rotational velocity as $W_{50,20}^i = 2V_{rot}$ (see Section 4.1).

Prior to the rotation curve derivation, the HI velocity fields were censored for skewed velocity profiles (high $h3$). A skewness of the velocity profiles might be present mostly due to beam-smearing and non-circular motions. Thus, censoring for high values of $h3$ allowed us to derive high-quality rotation curves, representing the actual rotational velocity of a galaxy as a function of radius, not affected by the effects mentioned above. Further details can be found in [Paper I](#).

6 THE TULLY-FISHER RELATIONS

In this section we present the statistical properties of the multi-wavelength TFRs using the different kinematic measures W_{50}^i , V_{max} and V_{flat} . We first discuss the fitting method. We then discuss the slope and vertical scatter (σ) of the TFRs and introduce the slope independent tightness (σ_\perp) of the TFRs. We conclude with a search for a 2nd parameter that may correlate with the residuals.

6.1 Fitting method

The study of the statistical properties of the TFR requires establishing the slope and zero point of the relation. However, there is no general agreement which fitting method is best suited. For example, it was shown that the slope of the TFR is affected by a Malmquist bias ([TC12](#)) which can be resolved by applying an inverse least squares regression ([Willick 1994](#)). Moreover, it is important to note that the vertical scatter of the TFR, which is crucial for the distance measure, is highly dependent on the slope. Thus, an intrinsically tight TFR may introduce a larger vertical scatter due to

Band	Slope (Mag)			Slope (dex)		
	W_{50}^i	V_{max}	V_{flat}	W_{50}^i	V_{max}	V_{flat}
FUV	-7.12±0.86	-7.04±0.98	-7.87±1.27	2.36±0.38	2.32±0.37	2.59±0.47
NUV	-6.45±0.76	-6.36±0.86	-6.91±0.94	1.93±0.40	1.91±0.40	2.06±0.41
u	-6.06±0.64	-6.30±0.60	-6.95±0.67	1.69±0.44	1.75±0.46	1.91±0.52
g	-6.11±0.33	-6.43±0.57	-7.12±0.6	1.9 ±0.33	1.97±0.4	2.17±0.44
r	-6.76±0.25	-7.09±0.51	-7.87±0.56	2.26±0.23	2.36±0.3	2.61±0.33
i	-7.02±0.32	-7.29±0.49	-8.14±0.57	2.12±0.38	2.19±0.44	2.42±0.49
z	-7.89±0.40	-8.17±0.52	-9.12±0.61	2.82±0.16	2.91±0.22	3.25±0.24
J	-8.73±0.52	-8.55±0.39	-9.22±0.4	3.23±0.26	3.16±0.20	3.41±0.19
H	-8.99±0.52	-8.83±0.42	-9.47±0.38	3.43±0.24	3.36±0.18	3.61±0.15
K ^s	-9.26±0.50	-9.08±0.41	-9.77±0.41	3.51±0.23	3.44±0.18	3.81±0.19
3.6 μm	-9.05±0.45	-8.86±0.37	-9.52±0.32	3.61±0.19	3.53±0.15	3.8 ±0.11
4.5μm	-9.04±0.46	-8.81±0.38	-9.51±0.33	3.52±0.19	3.45±0.16	3.7 ±0.12
Band	Zero Point (Mag)			Zero point (log(L(L _⊙)))		
	W_{50}^i	V_{max}	V_{flat}	W_{50}^i	V_{max}	V_{flat}
FUV	0.18±2.17	-0.09±2.44	1.77±3.12	7.53±0.95	7.66±0.93	7.05±1.16
NUV	-1.78±1.92	-2.07±2.15	-0.88±2.32	6.36±1.03	6.47±1	6.11±1.04
u	-2.45±1.62	-1.91±1.53	-0.41±1.71	4.71±1.13	4.59±1.2	4.21±1.32
g	-4.27±0.83	-3.55±1.42	-1.94±1.51	4.96±0.86	4.79±1.03	4.33±1.13
r	-3.24±0.63	-2.49±1.28	-0.67±1.39	4.28±0.59	4.07±0.78	3.49±0.84
i	-2.94±0.81	-2.32±1.25	-0.35±1.44	4.74±0.99	4.58±1.12	4.04±1.25
z	-0.87±1.01	-0.24±1.31	1.97±1.52	3.07±0.41	2.85±0.56	2.08±0.62
J	0.1 ±1.28	-0.44±0.99	1 ±0.99	1.92±0.67	2.13±0.52	1.59±0.49
H	0.08±1.29	-0.42±1.06	0.92±0.94	1.70±0.61	1.90±0.45	1.38±0.37
K ^s	0.52±1.24	0.00±1.04	1.44±0.038	1.58±0.6	1.78±0.46	1.22±0.44
3.6 μm	2.4±1.1	1.91±1.41	3.31±1.73	1.44±0.49	1.66±0.37	1.1±0.29
4.5μm	2.92±1.13	2.36±0.97	3.73±0.83	1.66±0.50	1.88±0.39	1.33±0.31

Table 3. The results of the orthogonal fits of the TFrs. Upper panel. Column (1): photometric band; Column (2)-Column(4): slopes of the TFrs based on W_{50}^i , V_{max} and V_{flat} , measured in magnitudes; Column (5)-Column(7): slope of the TFrs based on W_{50}^i , V_{max} and V_{flat} , measured in dex. Lower panel. Column (1): photometric band; Column (2)-Column(4): zero points of the TFrs based on W_{50}^i , V_{max} and V_{flat} , measured in magnitudes; Column (5)-Column(7): zero points of the TFrs based on W_{50}^i , V_{max} and V_{flat} , measured in dex.

Band	σ (Mag)			σ (dex)		
	W_{50}^i	V_{max}	V_{flat}	W_{50}^i	V_{max}	V_{flat}
FUV	0.87±0.14	0.89±0.15	0.97±0.17	0.30±0.09	0.31±0.09	0.33±0.1
NUV	0.74±0.13	0.76±0.14	0.77±0.15	0.25±0.09	0.26±0.09	0.26±0.09
u	0.44±0.15	0.47±0.14	0.44±0.15	0.19±0.11	0.19±0.12	0.19±0.12
g	0.27±0.11	0.34±0.14	0.32±0.14	0.14±0.1	0.15±0.11	0.15±0.11
r	0.22±0.09	0.31±0.13	0.29±0.13	0.12±0.08	0.14±0.1	0.13±0.1
i	0.25±0.1	0.3 ±0.12	0.31±0.13	0.11±0.06	0.12±0.08	0.12±0.08
z	0.29±0.11	0.32±0.13	0.33±0.14	0.12±0.07	0.13±0.08	0.13±0.09
J	0.39±0.11	0.4 ±0.09	0.39±0.09	0.15±0.08	0.16±0.07	0.15±0.06
H	0.41±0.11	0.44±0.1	0.38±0.09	0.16±0.07	0.17±0.06	0.15±0.06
K	0.41±0.1	0.44±0.1	0.40±0.09	0.16±0.07	0.17±0.06	0.16±0.06
3.6	0.39±0.1	0.41±0.09	0.33±0.08	0.15±0.06	0.16±0.05	0.13±0.05
4.5	0.40±0.1	0.42±0.09	0.34±0.08	0.16±0.06	0.16±0.05	0.13±0.05

Table 4. Vertical scatter of the TFrs in different photometrical bands measured in magnitudes and in dex. Column (1): photometric band; Column (2)-Column(4): scatters of the TFrs based on W_{50}^i , V_{max} and V_{flat} , measured in magnitudes; Column (5)-Column(7): tightnesses of the TFrs based on W_{50}^i , V_{max} and V_{flat} , measured in dex.

a steeper slope (Verheijen 2001). As we are interested in the tightness of the TFr, while the Malmquist bias is minimal for our sample, we apply an orthogonal regression where the best-fit model minimises the orthogonal distances from the points to the line. We apply a fitting method allowing for *bivariate correlated errors and an intrinsic scatter* (BCES, Akritas & Bershady 1996), using the python implementation developed by Nemmen et al. (2012). The main advantages of this method are that it takes errors in both directions into account, it permits the measurement errors of both variables to be dependent (for example uncertainties due to the incli-

nation) and it assigns less weight to outliers and data points with large errors.

In order to accurately calculate the (intrinsic) scatter and tightness of the relations, the following measurement uncertainties were taken into account:

- (i) the errors in total magnitudes $M_T^b, i(\lambda)$ due to the sky background, distance uncertainties and the uncertainty in the photometric zero-point.
- (ii) the errors on the rotational velocity measures V_{max} , V_{flat} and W_{50}^i , see Table 2.
- (iii) the error on the kinematic inclination which affects

Band	σ_{\perp} (dex)		
	W_{50}^i	V_{max}	V_{flat}
FUV	0.12±0.045	0.124±0.022	0.122±0.022
NUV	0.12±0.048	0.123±0.024	0.117±0.024
u	0.099±0.062	0.099±0.031	0.091±0.031
g	0.068±0.044	0.071±0.022	0.066±0.022
r	0.05±0.03	0.055±0.015	0.05±0.015
i	0.042±0.018	0.044±0.009	0.041±0.009
z	0.043±0.02	0.045±0.01	0.042±0.01
J	0.047±0.016	0.049±0.013	0.045±0.013
H	0.047±0.015	0.050±0.012	0.042±0.012
K	0.046±0.022	0.049±0.011	0.042±0.011
3.6	0.043±0.019	0.046±0.01	0.036±0.01
4.5	0.044±0.02	0.047±0.01	0.036±0.01

Table 5. Tightness of the TFRs in different photometric bands measured in dex. Column (1): photometric band; Column (2)-Column(4): tightness of the TFRs based on W_{50}^i , V_{max} and V_{flat} , measured in dex;

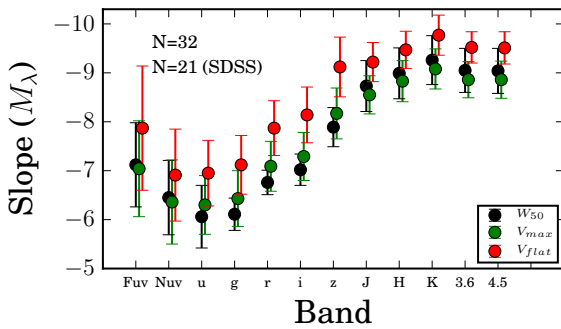


Figure 7. Slope of the TFR as a function of wavelength, calculated using different rotation measures. With black points indicated slopes measured for the TFR based on W_{50}^i , with green based on V_{max} and with red based on V_{flat} . Independently of band, the TFR based on V_{flat} demonstrates the steepest slope.

both the internal extinction correction and the kinematic measure, introducing covariance in the errors.

6.2 Slope, scatter and tightness

We measure the slope, scatter and tightness of the TFRs in 12 different bands with different kinematic measures, using the weighted orthogonal regression fit and taking correlated errors in both directions into account. It is important to point out that the comparisons are made for the samples with different numbers of galaxies: 32 for the UV and IR bands and 21 for the SDSS bands (see Section 3). However, we present the comparisons for the SDSS subsample of 21 galaxies for all bands in Appendix A.

It has been suggested for some time that the slope of the TFR steepens from blue to red wavelengths (Aaronson et al. 1979; Tully et al. 1982; Verheijen 2001). We confirm this result by our study, which covers a much broader wavelength range. The variation of the slope with passband is presented in Figure 7. Our result suggests that the slope as a function of wavelength in the mid-infrared bands stays more or less constant. Moreover, the TFR based on V_{flat} is always showing the steepest slope in every passband (Fig-

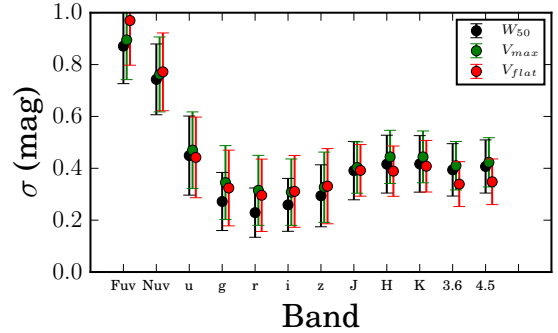


Figure 8. The vertical scatter of the TFR as a function of wavelength, calculated using different rotation measures. With black points indicating the scatter measured for the TFR based on W_{50}^i , with green based on V_{max} and with red based on V_{flat} .

ure 7). The steepest slope is found in the K -band and is consistent with -10 mag or 4 dex.

The vertical scatter (σ) in every passband was measured using each of the three velocity measures W_{50}^i , V_{max} and V_{flat} . The total observed scatter was calculated according to the following equation:

$$\sigma = \sqrt{\frac{\chi^2}{N-1}}, \quad (5)$$

where χ^2 is

$$\sum (M_T^{b,i} - (a \times \log(V_{circ}) + b))^2,$$

and where V_{circ} stands for one of the three velocity measures W_{50}^i , $2V_{max}$ or $2V_{flat}$, a and b are the fitted slope and zero point of the relation respectively, and $N-1$ is the number of degrees of freedom. Errors on the scatter were estimated following a full error propagation calculation. The vertical scatter in magnitudes, which is relevant for distance measurements, is shown in Figure 8 as a function of wavelength. It is clear from Figure 8 that the vertical scatter is roughly constant in the mid-IR bands, suggesting that there might be no preference for which mid-IR band to use as a distance indicator. Therefore, preference should be given to the one which suffers least from dust extinction and non-stellar contamination. However, one can argue that the r -band TFR based on W_{50}^i should be used as a distance estimation tool, since it demonstrates the smallest vertical scatter. Interestingly, Verheijen (2001) had found a very similar result. Yet, it is important to keep in mind that the vertical scatter is a slope-dependent measure, and an intrinsically tight TFR will demonstrate a large vertical scatter if the slope of the relation is steep. Moreover, it is remarkable that for the UV and optical bands (FUV to z) the vertical scatter may be smaller when the relation is based on W_{50}^i , with the smallest scatter of $\sigma = 0.23$ mag in the r band. However, for the redder bands (J to $4.5\mu m$) the smallest vertical scatter $\sigma = 0.33$ mag is found in the $3.6\mu m$ band TFR based on $2V_{flat}$. This is due to the fact that when the relation is based on $2V_{flat}$, the slope steepens more significantly for the UV and optical bands than for the infrared.

The tightness (σ_{\perp}) of the TFR is the perpendicular scatter between the data points and the linear model, which provides information on how “tight” the data are spread around

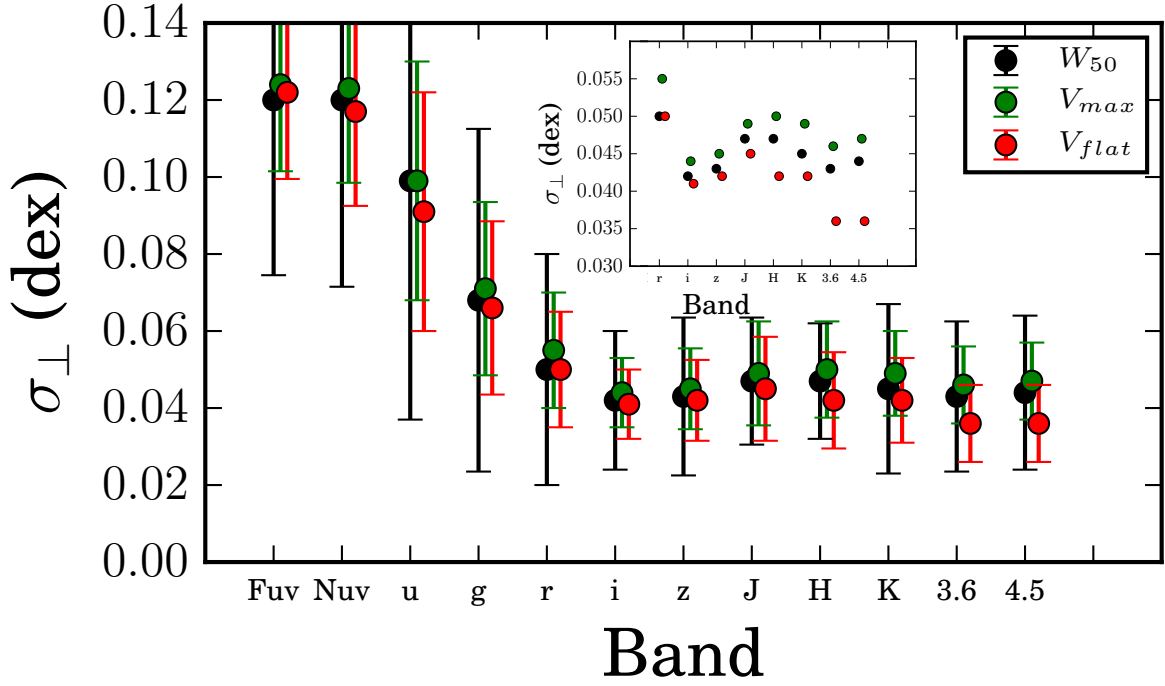


Figure 9. Orthogonal tightness of the TFR as a function of wavelength, calculated using different rotation measures. With black points indicated the scatter measured for the TFR based on W_{50}^i , with green based on V_{max} and with red based on V_{flat} . Independently of wavelength the relation is “tighter” when it is based on V_{flat} as a rotation measure. The inset demonstrates the zoom-in to the infra-red bands.

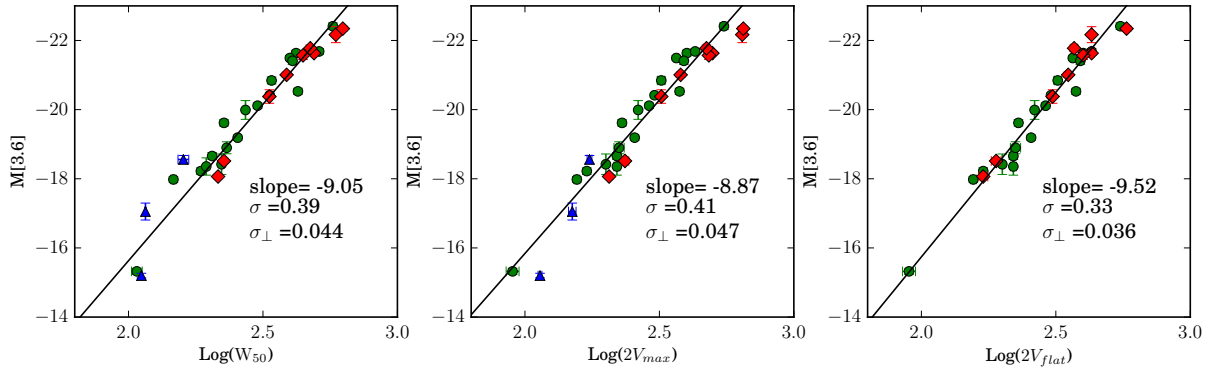


Figure 10. The $3.6 \mu\text{m}$ TFRs based on the different kinematic measures W_{50}^i – left, V_{max} – middle and V_{flat} – right. Green symbols show flat rotation curves ($V_{max} = V_{flat}$), and red symbols indicate galaxies with declining rotation curves ($V_{max} > V_{flat}$). Blue symbols indicate galaxies with rising rotation curves ($V_{max} < V_{flat}$). These galaxies were not included when fitting the model.

the regression line. It is slope independent and has been recently used for testing galaxy formation and evolution models (Papastergis et al. 2016). Therefore, the tightness provides important information on the intrinsic properties of the TFR. We calculate tightness using the following formula:

$$\sigma_{\perp} = \sqrt{\frac{\sum d_i^2}{N-2}}, \quad (6)$$

where $N-2$ is the amount of degrees of freedom and d_i is the perpendicular distance of each point to a model line:

$$d_i = \sqrt{\left(\frac{x_i + ay_i - ab}{a^2 + 1} - x_i\right)^2 + \left(a \times \frac{x_i + ay_i - ab}{a^2 + 1} + b - y_i\right)^2},$$

here x_i and y_i are the coordinates of each measured point, in our case $\log(L_{\lambda}/L_{\odot})$ and $\log(V_{circ})$ respectively, while a and b are the slope and the zero point of a model line. Errors on the tightness were estimated following a full error propagation calculation. The tightness of the TFR as a function of wavelength is shown in Figure 9. It is also roughly constant in the mid-IR bands with the tightest correlation at $3.6 \mu\text{m}$ equal to $\sigma_{\perp} = 0.036$ dex. Moreover, independently of the

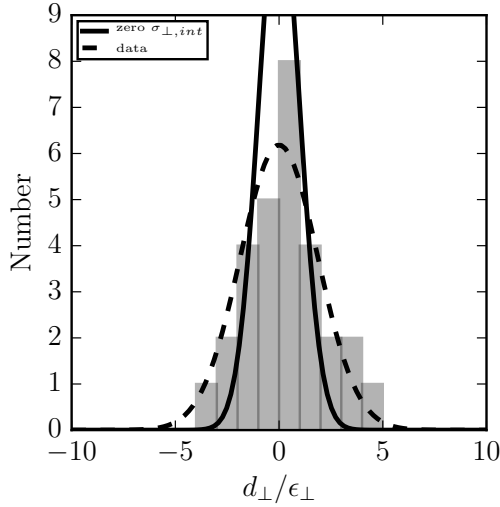


Figure 11. Histogram of the perpendicular distances from the data points to the line ($d_{\perp,i}$) in the $L_{[3.6]}^{T,b,i}(L_{\odot})-V_{flat}$ relation, normalised by the perpendicular errors $\epsilon_{\perp,i}$. The standard normal distribution, which would be expected for a zero intrinsic tightness is shown with a black line. The best-fit to the data, weighted by the Poisson errors, is shown with the dashed line with a standard deviation of 1.87 ± 0.13 .

photometric band, the TFRs tend to be somewhat tighter when based on $2V_{flat}$ (Figure 9). The values of the statistical properties of the TFRs (slope, zero point, scatter and tightness) can be found in Tables 3, 4 and 5.

6.3 A closer look at the $3.6 \mu\text{m}$ TFR

Figure 10 shows the TFR in the $3.6 \mu\text{m}$ band based on W_{50}^i , V_{max} and V_{flat} . According to our fit, the $M_{[3.6]}^{T,b,i}-V_{flat}$ correlation can be described as :

$$M_{[3.6]}^{T,b,i} = (-9.52 \pm 0.32) \times \log(2V_{flat}) + 3.3 \pm 0.8 \quad (7)$$

and the $L_{[3.6]}^{T,b,i}(L_{\odot})-V_{flat}$ correlation as

$$\log(L_{[3.6]}^{T,b,i}) = (3.7 \pm 0.11) \times \log(2V_{flat}) + 1.3 \pm 0.3, \quad (8)$$

based on $M_{\odot}(3.6\mu\text{m}) = 3.24 \text{ mag}$ (Oh et al. 2008). Here $M_{[3.6]}^{T,b,i}$ is the total magnitude, corrected for Galactic and internal extinction, $L_{[3.6]}^{T,b,i}$ is the luminosity, presented in solar luminosities, and V_{flat} is the rotational velocity of the flat part of the extended HI rotation curve in km/s .

Eqn. 7 and Eqn. 8 describe the tightest of the TFRs, with an observed tightness equal to $\sigma_{\perp,obs} = 0.036 \pm 0.010$ dex. Without considering the observational errors, $\sigma_{\perp,obs}$ presents an upper limit on the intrinsic tightness of the TFR $_{[3.6]-V_{flat}}$ of $\sigma_{\perp,int} < \sigma_{\perp,obs} = 0.036$ dex. This is 0.02 dex smaller than the observed tightness of the Baryonic TFR for gas-rich galaxies, found by Papastergis et al. (2016), using W_{50}^i as a rotational velocity measure.

Further, we can estimate the intrinsic tightness of the TFR $_{[3.6],V_{flat}}$ by comparing the perpendicular distance from each data point to the model line $d_{\perp,i}$ taking into account the measurement error $\epsilon_{\perp,i}$, where $\epsilon_{\perp,i}$ is based on the observational errors on the luminosity ($\epsilon_{L_{[3.6],i}}$) and on the

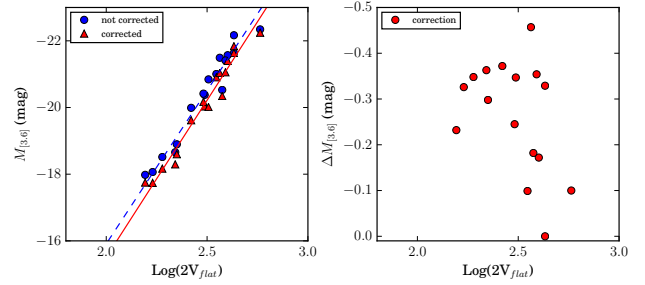


Figure 12. Left panel: The $M_{[3.6]}^{T,b,i}-V_{flat}$ relation is shown with blue points. The relation using total magnitudes corrected for non-stellar contamination is shown with red points. Right panel: The correction for non-stellar contamination as a function of rotational velocity $2V_{flat}$.

rotational velocity ($\epsilon_{V_{flat},i}$) of each data point, projected onto the direction perpendicular to the model line:

$$\epsilon_i^2 = (\epsilon_{\log(L_{[3.6],i})} \times \frac{1}{\sqrt{1+a^2}})^2 + (\epsilon_{\log(2V_{flat},i)} \times \frac{a}{\sqrt{1+a^2}})^2, \quad (9)$$

where a is the slope of the line. The uncertainty on to the distance measurement is included in the error on the total luminosity. For more details on the derivation of Eqn. 9 see Papastergis et al. 2016 (Appendix B). If the observed tightness of the relation would be only due to the measurement errors, the histogram of $d_{\perp,i}/\epsilon_{\perp,i}$ would then follow a standard normal distribution. Yet, it is clear from Figure 11 that the spread of $d_{\perp,i}/\epsilon_{\perp,i}$ is larger than expected from a standard normal distribution, with a measured standard deviation of 1.87 ± 0.13 (dashed curve). Therefore, a small but non-zero intrinsic perpendicular scatter (σ_{\perp}) is present in the TFR $_{[3.6]-V_{flat}}$.

To obtain the best estimate for the intrinsic tightness, we present it as follows :

$$\sigma_{\perp,int} = \sqrt{\sigma_{\perp,obs}^2 - \sigma_{\perp,err}^2}, \quad (10)$$

where $\sigma_{\perp,err} = 0.025$ dex is the perpendicular scatter due to the measurement errors only. Thus, we obtain an estimate for the intrinsic perpendicular scatter $\sigma_{\perp,int} \sim 0.026$ dex. It is important to keep in mind that this result depends on how accurately the observational errors can be determined. Therefore, any underestimate of the observational errors will lead to a decrease of the intrinsic tightness and vice versa.

As was already mentioned before, previous studies (Meidt et al. 2012; Querejeta et al. 2015) concluded that Spitzer $3.6 \mu\text{m}$ luminosities represent not only the old stellar population. Up to 30% of the $3.6 \mu\text{m}$ light might be coming from warm dust which is heated by young stars and re-emitted at longer wavelengths. Moreover, asymptotic giant branch (AGB) stars appear to peak at $3.6 \mu\text{m}$ as well. To test the effect of contamination by dust and/or AGB stars on the tightness of the TFR, we constructed a subsample of 18 galaxies which were studied as part of the S⁴G analysis by Querejeta et al. (2015). In this study, the $3.6 \mu\text{m}$ images were decomposed into stellar and non-stellar contributions using an Independent Component Analysis described in Meidt et al. (2012). We compared the statistical properties of the TFRs in the observed $3.6 \mu\text{m}$ band and in the $3.6 \mu\text{m}$ band corrected for non-stellar contamination, as demonstrated in

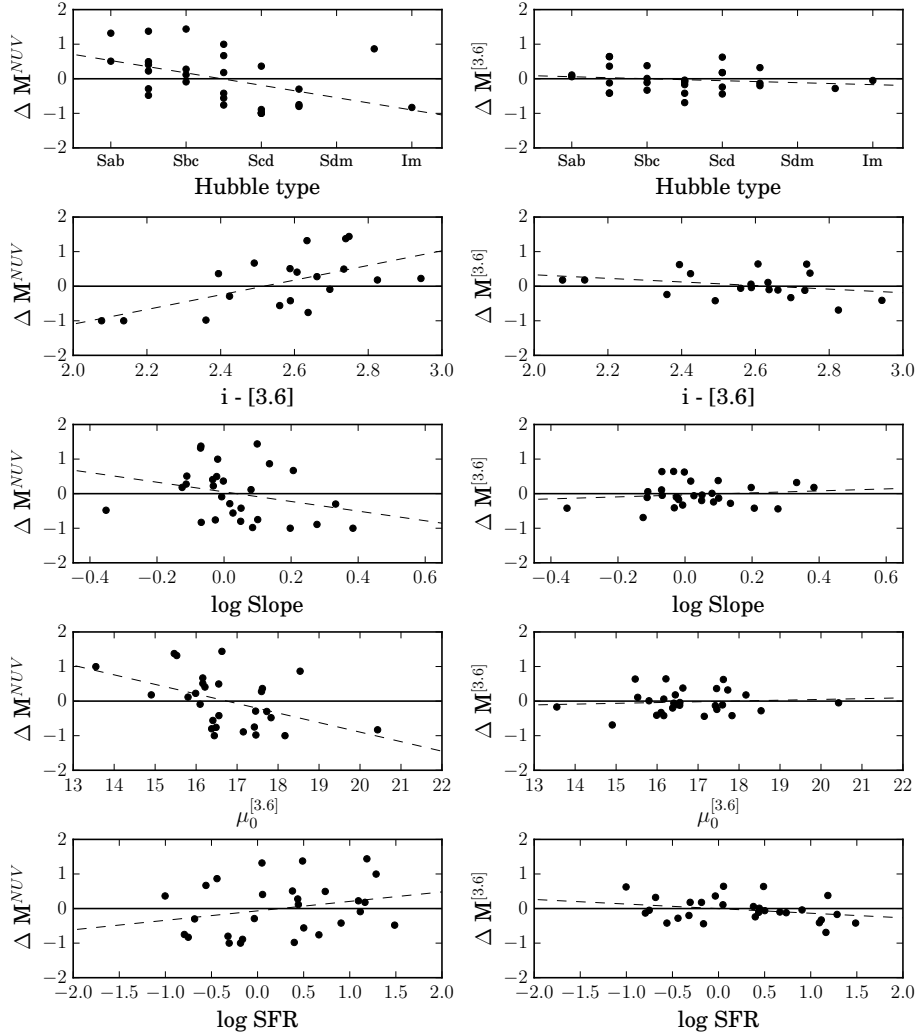


Figure 13. Residuals of the $M_\lambda - V_{flat}$ TFrs in the NUV and $3.6 \mu\text{m}$ bands as a function of global galactic properties.

Figure 12 (left panel). The results of the comparison can be found in Table 6. It is clear that the scatter and tightness of the TFR at $3.6 \mu\text{m}$ can be slightly reduced if the non–stellar contamination is corrected for, especially when the TFR is based on V_{flat} as a rotational velocity measure. The very weak correlation between the correction for non–stellar contamination and rotational velocity (Figure 12, right panel) results in a slight steepening of the TFR slope. However, the difference in the scatter ($\Delta\sigma = 0.03 \text{ mag}$) and tightness ($\Delta\sigma_\perp = 0.004 \text{ dex}$) is too small ($\sim 10\%$) to draw definite conclusions. Hence, a more detailed study of this subject should be done with a larger sample of galaxies for which a decomposition into stellar and non–stellar emission has been performed.

6.4 Need for a 2nd parameter?

For many decades it was suggested that the scatter in the TFR can be reduced by adding a second parameter such as colour, morphological type or velocity dispersion (Rubin et al. 1985; Tully & Pierce 2000; Cortese et al. 2014). This parameter is usually derived from the correlations of the

N=19	Observed			Corrected		
	W_{50}^i	V_{max}	V_{flat}	W_{50}^i	V_{max}	V_{flat}
slope (mag)	-8.52	-8.56	-9.20	-8.77	-8.77	-9.47
σ (mag)	0.40	0.45	0.32	0.38	0.41	0.29
σ_\perp (dex)	0.043	0.046	0.036	0.043	0.046	0.031

Table 6. Slope, scatter and tightness of the TFrs, constructed for 19 galaxies in the observed $3.6 \mu\text{m}$ band and in the $3.6 \mu\text{m}$ band, corrected for the non–stellar contamination. Column(1): name of the parameter; Column (2-4): slope, scatter and tightness of the TFrs in the observed $3.6 \mu\text{m}$ band (based on different velocity measures); Column (5-7): slope, scatter and tightness of the TFrs in the $3.6 \mu\text{m}$ band, corrected for non–stellar emission (based on different velocity measures);

residuals of the TFR with global galactic properties. It has been shown that the residuals of the TFR based on W_{50}^i correlate well with the colour or morphological type of galaxies (Aaronsen & Mould 1983; Rubin et al. 1985; Russell 2004). The correlations are usually found in the blue bands which tend to have much larger scatter, and found to be completely absent in the red bands where the scatter is already very small (Tully & Pierce 2000; Verheijen 2001). However,

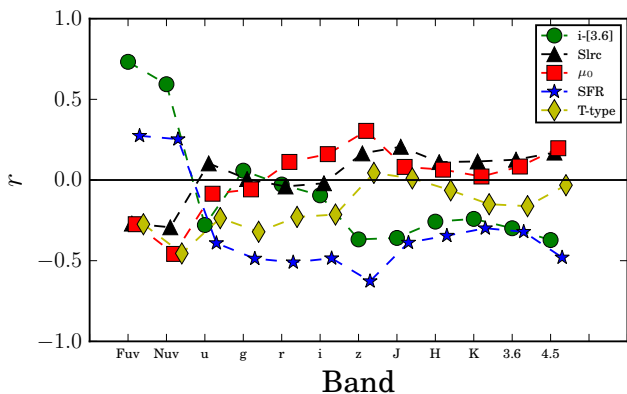


Figure 14. Pearson’s correlation coefficients between $M_T(\lambda) - \log(2V_{flat})$ and global galactic properties as a function of wavelength.

Sorce et al. (2012) found a colour term present in the residuals of the $3.6 \mu\text{m}$ TFR, which allowed them to reduce the observed scatter by 0.05 mag.

We examine the residuals ΔM_λ of the TFRs in each band based on V_{flat} , and investigate possible correlations with global galactic properties such as star formation rate (SFR), central surface brightness, and the outer slope of the rotation curve. First, we consider in detail two extremes ΔM_{NUV} and $\Delta M_{[3.6]}$ based on V_{flat} . From Figure 13 it is clear that while NUV residuals show hints for correlations with all galactic parameters, these hints completely disappear for the $3.6 \mu\text{m}$ residuals.

To quantitatively describe the strengths of the correlations between TFR residuals and global galactic properties, we calculate Pearson’s coefficients r , a measure of the linear correlation between two variables. Figure 14 shows the Pearson’s coefficients r as a function of wavelength for the correlations between ΔM^λ and various galactic properties such as $i - [3.6]$ colour, the outer slope of the rotation curve (see Section 5.2), central surface brightness at $3.6 \mu\text{m}$, star formation rate and morphological type. It is clear from Figure 14 that the Pearson’s coefficients do not suggest any strong correlations between residuals of the TFRs and various galactic properties in any band, except for the *FUV* where a prominent correlation with the $i - [3.6]$ colour is found. This result is in agreement with previous studies for blue bands. However, there is no evidence for a significant correlation between $\Delta M_{[3.6]}$ and the $i - [3.6]$ colour ($r = -0.29$), despite the previous suggestions by Sorce et al. (2012). Nonetheless, the strength for the correlation between $\Delta M_{[3.6]}$ and the $i - [3.6]$ colour was not presented in the Sorce et al. (2012) study, therefore we can not perform a quantitative comparison. In conclusion, we do not find any second parameter, which would help to reduce the scatter in the near-infrared TFR.

7 SUMMARY AND CONCLUSIONS

In this paper, we present an empirical study of the multi-wavelength Tully–Fisher relation, taking advantage of spatially resolved HI kinematics. This study aims to investi-

gate the statistical properties of the TFRs in 12 photometric bands, using three rotational velocity measures: W_{50}^i from the global HI profile, and V_{max} and V_{flat} from high-quality, spatially-resolved HI rotation curves. The galaxies in our sample were selected to have independently measured Cepheid or/and TRGB distances. This allowed us to calibrate the TFR with minor distance uncertainties ($\sigma_{dist} = 0.07$ mag, instead of $\sigma_{dist} = 0.41$ mag when using Hubble flow distances).

First, we present a slope-independent perpendicular scatter (σ_\perp) of the TFR, which describes how tight the data points are spread around the model line. We study the tightness as a function of wavelength for TFRs based on different rotational velocity measures (Section 6.2). We find that the tightness σ_\perp of the TFR improves significantly from the blue to the infrared bands, but it levels off for the near-infrared bands, with the largest $\sigma_\perp = 0.043$ dex in the H-band and the smallest $\sigma_\perp = 0.036$ dex in the $3.6 \mu\text{m}$ band, using V_{flat} as a rotational velocity measure. We find that the latter is not consistent with a zero intrinsic perpendicular scatter indicating that the measured $\sigma_{\perp,obs}$ can not be completely explained by the measurement errors (see Section 6.3). Nevertheless, the TFR based on the $3.6 \mu\text{m}$ luminosities and V_{flat} provides the tightest constraint on theories of galaxy formation and evolution. Indeed, such a tight correlation between the $3.6 \mu\text{m}$ luminosity of a galaxy with the velocity of the outer most point of the rotation curve suggests an extremely tight correlation between the mass of the dark matter halo and its baryonic content. Certainly, $3.6 \mu\text{m}$ light has been considered as the best tracer of the total stellar mass of galaxies which dominates the baryonic mass. However, many observational studies have shown that not only old stars, but also hot dust and AGB stars might contribute to this light, up to 30% in some cases. We have shown that the observed tightness and scatter of the TFR can be somewhat reduced if the $3.6 \mu\text{m}$ light is corrected for non-stellar contamination (see Section 6.3). More studies should be done to further investigate this effect, using a larger sample of galaxies for which the decomposition of the light into old stars and contamination can be performed.

An obvious next step in studying the tightness of the TFR is to measure the slope, scatter and tightness of the baryonic TFR (BTFR) and compare this with measurements derived for the $3.6 \mu\text{m}$ band. This approach introduces more uncertainties related to estimating the stellar mass. For instance, Papastergis et al. (2016) found a larger perpendicular scatter of the BTFR, even though they considered a sample of heavily gas-dominated galaxies for which uncertainties in stellar mass are less significant. That study was done using only W_{50}^i as a rotational velocity measure. A forthcoming paper will discuss the statistical properties of the BTFR with resolved HI kinematics.

Next, we study the slope of the TFR as a function of wavelength, using W_{50}^i , V_{max} and V_{flat} (see Section 6.2). We confirm the results of previous studies (Aaronson et al. 1979; Tully et al. 1982; Verheijen 2001), that the slope of the TFR steepens toward longer wavelengths by broadening the study over a wider wavelength range. The steepening of the slope results from the fact that redder galaxies are much brighter than bluer galaxies at longer wavelengths. Galaxies that are bright in the infrared tend to rotate more rapidly. Therefore, at longer wavelengths the high-mass end of the

TFR will rise faster than the low-mass end. In addition, we find that the TFR based on V_{flat} as a rotational velocity measure has the steepest slope in every photometric band. Massive galaxies tend to have declining rotation curves with $V_{max} > V_{flat}$ (see Section 4.1, Figure 6). If V_{flat} is used as a rotation velocity measure, bright galaxies have lower velocities than when measured with W_{50}^i and/or V_{max} . This difference reduces the velocity range over which the galaxies are distributed. This effect steepens the slope of the TFR as well. Similar results were found by Verheijen (2001) and Noordermeer et al. (2007). Moreover, the use of V_{flat} “straightens” the TFR and removes a possible curvature in the TFR at the high-mass end (Neill et al. 2014; Noordermeer & Verheijen 2007).

Subsequently, we discussed the vertical scatter (σ) of the TFR as a function of wavelength, using three rotational velocity measures (see Section 6.2). It is well known, that the vertical scatter of the TFR is strongly dependent on the slope. Thus, even an intrinsically tight correlation can be found to have a large vertical scatter if the slope is steep. The vertical scatter of the TFR is mostly discussed in the context of determining distances to galaxies. We find the smallest vertical scatter in the r -band, using W_{50}^i as a rotational velocity measure, confirming the result found by Verheijen (2001). Moreover, we find that the vertical scatter in the $3.6 \mu\text{m}$ band ($\sigma = 0.39\text{mag}$) to be lower than previously reported by Sorce et al. (2012) for the $3.6 \mu\text{m}$ band ($\sigma = 0.44\text{mag}$), and by Neill et al. (2014) for the $3.4 \mu\text{m}$ band ($\sigma = 0.54 \text{mag}$). These comparisons are done using W_{50}^i as a rotational velocity measure. Besides, we find σ to be smaller when using W_{50}^i as a velocity measure for the FUV and optical bands ($FUV - z$). For the infrared bands (J to $4.5\mu\text{m}$), σ is smaller when the TFR is based on V_{flat} . This result suggests that σ in the infrared bands is less sensitive to the slope steepening with V_{flat} .

We searched for a second parameter that can possibly help to reduce the vertical scatter of the TFR. We considered the residuals of the TFRs ($\Delta M_{\lambda} - V_{flat}$) in every band (see Section 6.4) and find no significant correlations between the residuals of the TFRs and main galactic properties (SFR, central surface brightness, outer slope of the rotation curve, morphological type and $i - [3.6]$ colour, see Figure 14). Even though the UV bands show hints for correlations between the residuals and some of the global properties such as SFR (see Figure 13), no correlations are found in the red bands. This suggests that these correlations are triggered by different stellar populations in early-type and late-type galaxies of the same UV luminosity and not by the difference in V_{flat} governed by the dark matter halo. Lastly, it is important to mention that we do not find any correlation between the TFR residuals $\Delta M_{[3.6]} - W_{50}^i$ and the colour term $i - [3.6]$ (Pearson’s coefficient $r = 0.1$), contrary to the result reported previously by Sorce et al. (2012).

As was shown by Sorce & Guo (2016), the size of the sample may have a significant impact on the scatter of the TFR. Therefore, it is necessary to point out that the limited size of our sample might contribute to the uncertainties in the slope, scatter and zero point of the TFRs. However, it is very expensive to establish a large sample of spiral galaxies which have both independently measured distances and resolved HI kinematics. Nonetheless, this challenge will be possible to meet with the HI imaging surveys that are planned

for new observational facilities, such as Apertif (Verheijen et al. 2008), MeerKAT (de Blok et al. 2009) and ASKAP (Johnston et al. 2007), providing resolved HI kinematics for many thousands of galaxies.

ACKNOWLEDGEMENTS

AP is grateful to Emmanouil Papastergis for fruitful discussions and useful comments. AB acknowledges financial support from the CNES (Centre National d’Etudes Spatial – France). We thank the staff of the GMRT who made our observations possible. The GMRT is run by the National Centre for Radio Astrophysics of the Tata Institute of Fundamental Research. This research has made use of the NASA/IPAC Extragalactic Database (NED) which is operated by the Jet Propulsion Laboratory, California Institute of Technology, under contract with the National Aeronautics and Space Administration. This research made use of Montage, funded by the National Aeronautics and Space Administration’s Earth Science Technology Office, Computational Technologies Project, under Cooperative Agreement Number NCC5-626 between NASA and the California Institute of Technology. The code is maintained by the NASA/IPAC Infrared Science Archive. We acknowledge financial support from the DAGAL network from the People Programme (Marie Curie Actions) of the European Union’s Seventh Framework Programme FP7/2007-2013/ under REA grant agreement number PITNGA-2011-289313. We acknowledge the Leids Kerkhoven–Bosscha Fonds (LKBF) for travel support.

REFERENCES

- Aaronson M., Mould J., 1983, *ApJ*, **265**, 1
 Aaronson M., Huchra J., Mould J., 1979, *ApJ*, **229**, 1
 Ahn C. P., et al., 2012, *ApJS*, **203**, 21
 Akritas M. G., Bershady M. A., 1996, *ApJ*, **470**, 706
 Begeman K. G., 1989, *A&A*, **223**, 47
 Bernstein G. M., Guhathakurta P., Raychaudhury S., Giovanelli R., Haynes M. P., Herter T., Vogt N. P., 1994, *AJ*, **107**, 1962
 Bosma A., 1981, *AJ*, **86**, 1791
 Broeils A. H., van Woerden H., 1994, *A&AS*, **107**
 Casertano S., van Gorkom J. H., 1991, *AJ*, **101**, 1231
 Cortese L., et al., 2014, *ApJ*, **795**, L37
 Courteau S., Andersen D. R., Bershady M. A., MacArthur L. A., Rix H.-W., 2003, *ApJ*, **594**, 208
 Courtois H. M., Tully R. B., 2012, *ApJ*, **749**, 174
 Courtois H. M., Tully R. B., Héraudeau P., 2011, *MNRAS*, **415**, 1935
 Freedman W. L., et al., 2001, *ApJ*, **553**, 47
 Johnston S., et al., 2007, *Publ. Astron. Soc. Australia*, **24**, 174
 Macciò A. V., Udrescu S. M., Dutton A. A., Obreja A., Wang L., Stinson G. R., Kang X., 2016, *MNRAS*, **463**, L69
 Martin D. C., et al., 2005, *ApJ*, **619**, L1
 Meidt S. E., et al., 2012, *ApJ*, **744**, 17
 Navarro J. F., Steinmetz M., 2000, *ApJ*, **538**, 477
 Neill J. D., Seibert M., Tully R. B., Courtois H., Sorce J. G., Jarrett T. H., Scowcroft V., Masci F. J., 2014, *ApJ*, **792**, 129
 Nemmen R. S., Georganopoulos M., Guiriec S., Meyer E. T., Gehrels N., Sambruna R. M., 2012, *Science*, **338**, 1445
 Noordermeer E., 2006, PhD thesis, Groningen: Rijksuniversiteit
 Noordermeer E., Verheijen M. A. W., 2007, *MNRAS*, **381**, 1463

- Noordermeer E., van der Hulst J. M., Sancisi R., Swaters R. S., van Albada T. S., 2007, *MNRAS*, **376**, 1513
- Oh S.-H., de Blok W. J. G., Walter F., Brinks E., Kennicutt Jr. R. C., 2008, *AJ*, **136**, 2761
- Papastergis E., Adams E. A. K., van der Hulst J. M., 2016, *A&A*, **593**, A39
- Peletier R. F., Willner S. P., 1991, *ApJ*, **382**, 382
- Pizagno J., et al., 2007, *AJ*, **134**, 945
- Ponomareva A. A., Verheijen M. A. W., Bosma A., 2016, *MNRAS*, **463**, 4052
- Querejeta M., et al., 2015, *ApJS*, **219**, 5
- Rizzi L., Tully R. B., Makarov D., Makarova L., Dolphin A. E., Sakai S., Shaya E. J., 2007, *ApJ*, **661**, 815
- Rubin V. C., Burstein D., Thonnard N., 1980, *ApJ*, **242**, L149
- Rubin V. C., Burstein D., Ford Jr. W. K., Thonnard N., 1985, *ApJ*, **289**, 81
- Russell D. G., 2004, *ApJ*, **607**, 241
- Schaye J., et al., 2015, *MNRAS*, **446**, 521
- Sheth K., et al., 2010, *PASP*, **122**, 1397
- Skrutskie M. F., et al., 2006, *AJ*, **131**, 1163
- Sorce J. G., Guo Q., 2016, *MNRAS*, **458**, 2667
- Sorce J. G., Courtois H. M., Tully R. B., 2012, *AJ*, **144**, 133
- Sorce J. G., et al., 2013, *ApJ*, **765**, 94
- Spekkens K., Giovanelli R., 2006, *AJ*, **132**, 1426
- Swaters R. A., van Albada T. S., van der Hulst J. M., Sancisi R., 2002, *A&A*, **390**, 829
- Swaters R. A., Sancisi R., van Albada T. S., van der Hulst J. M., 2009, *A&A*, **493**, 871
- Tully R. B., Courtois H. M., 2012, *ApJ*, **749**, 78
- Tully R. B., Fisher J. R., 1977, *A&A*, **54**, 661
- Tully R. B., Pierce M. J., 2000, *ApJ*, **533**, 744
- Tully R. B., Mould J. R., Aaronson M., 1982, *ApJ*, **257**, 527
- Tully R. B., Verheijen M. A. W., Pierce M. J., Huang J.-S., Waincoat R. J., 1996, *AJ*, **112**, 2471
- Tully R. B., Rizzi L., Shaya E. J., Courtois H. M., Makarov D. I., Jacobs B. A., 2009, *AJ*, **138**, 323
- Verheijen M. A. W., 2001, *ApJ*, **563**, 694
- Verheijen M. A. W., Sancisi R., 2001, *A&A*, **370**, 765
- Verheijen M. A. W., Oosterloo T. A., van Cappellen W. A., Bakker L., Ivashina M. V., van der Hulst J. M., 2008, in Minchin R., Momjian E., eds, American Institute of Physics Conference Series Vol. 1035, The Evolution of Galaxies Through the Neutral Hydrogen Window. pp 265–271 ([arXiv:0806.0234](https://arxiv.org/abs/0806.0234)), doi:10.1063/1.2973599
- Vogelsberger M., et al., 2014, *MNRAS*, **444**, 1518
- Weiner B. J., Sellwood J. A., Williams T. B., 2001, *ApJ*, **546**, 931
- Werner M. W., et al., 2004, *ApJS*, **154**, 1
- Willick J. A., 1994, *ApJS*, **92**, 1
- de Blok E., Booth R., Frank B., 2009, in Proceedings of Panoramic Radio Astronomy: Wide-field 1-2 GHz Research on Galaxy Evolution. p. 7
- de Blok W. J. G., et al., 2014, *A&A*, **566**, A80
- de Jong R. S., 1996, *A&AS*, **118**, 557
- van Albada T. S., Bahcall J. N., Begeman K., Sancisi R., 1985, *ApJ*, **295**, 305

APPENDIX A: TFRS FOR THE SDSS SUBSAMPLE

In this Appendix we present the results for the smaller SDSS sample. In this subsample we consider only 21 galaxies which have photometry from all 12 bands. This allows us to compare the slope, scatter and tightness of the TFRs at various wavelengths for the same number of galaxies. We recall that the lack of SDSS data for our full sample resulted in this smaller SDSS subsample. Figure A1 demonstrates the slope,

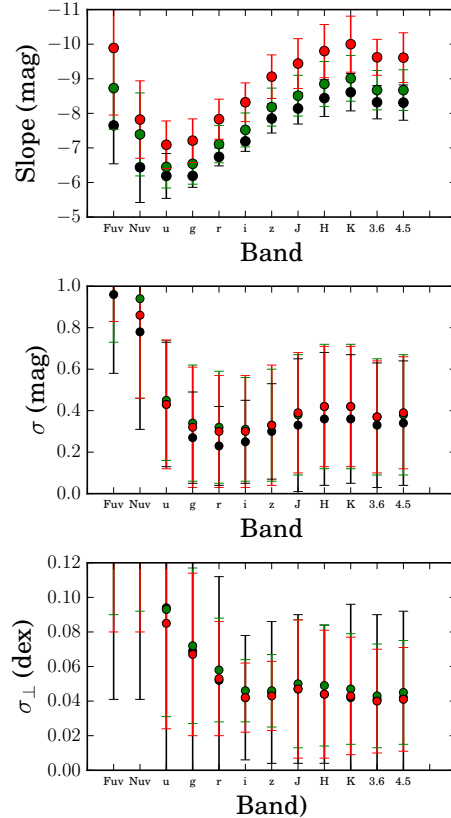


Figure A1. Slope, scatter and tightness of the TFR of the SDSS subsample as a function of wavelength, calculated using different rotation measures. With black points indicated values measured for the TFR based on W_{50}^i , with green based on V_{max} and with red based on V_{flat} .

scatter and tightness of the TFRs for this subsample. Even though the number of galaxies is smaller, there is no significant difference in trends compared to results based on the full sample. Table A1 summarises the measurements for the reduced TFR sample.

APPENDIX B: TFRS, USING 2.2H MAGNITUDES

In this Appendix we briefly present the results of the TFRs, based on magnitudes measured within 2.2 disk scale lengths. Figure B1 demonstrates the slope, scatter and tightness of these TFRs. It is clear from the figures, that even though the trends remain the same, the errors on the scatter and tightness significantly increase. Moreover, usage of magnitudes measured within 2.2 disk scale lengths did not decrease the scatter or improve the tightness of the TFRs in comparison with total magnitudes. Table B1 summarises the measurements for the TFRs, based on 2.2h magnitudes.

Band	Slope (Mag)			Scatter (Mag)			Tightness σ_{\perp} (dex)		
	W_{50}^i	V_{max}	V_{flat}	W_{50}^i	V_{max}	V_{flat}	W_{50}^i	V_{max}	V_{flat}
FUV	-7.65±1.11	-8.73±1.20	-9.89±1.94	0.96±0.38	1.13±0.40	1.17±0.34	0.132±0.091	0.135±0.045	0.125±0.045
NUV	-6.44±1.02	-7.39±1.20	-7.82±1.12	0.78±0.47	0.94±0.48	0.86±0.40	0.138±0.097	0.141±0.049	0.129±0.049
u	-6.19±0.65	-6.45±0.61	-7.09±0.69	0.43±0.30	0.45±0.29	0.43±0.31	0.094±0.124	0.093±0.062	0.085±0.061
g	-6.19±0.33	-6.54±0.59	-7.21±0.63	0.27±0.22	0.34±0.28	0.32±0.29	0.069±0.089	0.072±0.045	0.067±0.047
r	-6.74±0.26	-7.11±0.54	-7.83±0.58	0.23±0.19	0.32±0.27	0.30±0.27	0.052±0.060	0.058±0.030	0.053±0.033
i	-7.19±0.29	-7.52±0.49	-8.32±0.56	0.25±0.20	0.31±0.25	0.30±0.27	0.042±0.036	0.046±0.018	0.042±0.020
z	-7.85±0.42	-8.18±0.55	-9.06±0.63	0.30±0.23	0.33±0.27	0.33±0.29	0.045±0.041	0.046±0.021	0.043±0.020
J	-8.14±0.45	-8.51±0.59	-9.44±0.72	0.33±0.32	0.38±0.29	0.39±0.29	0.047±0.043	0.050±0.037	0.047±0.040
H	-8.44±0.53	-8.85±0.65	-9.80±0.77	0.36±0.32	0.42±0.30	0.42±0.29	0.044±0.040	0.049±0.035	0.044±0.037
K	-8.61±0.54	-9.01±0.66	-10.0±0.81	0.36±0.31	0.42±0.30	0.42±0.29	0.042±0.054	0.047±0.032	0.043±0.034
3.6	-8.32±0.48	-8.67±0.57	-9.62±0.52	0.33±0.30	0.37±0.28	0.37±0.27	0.041±0.049	0.043±0.030	0.040±0.030
4.5	-8.31±0.51	-8.67±0.59	-9.61±0.72	0.34±0.30	0.38±0.29	0.39±0.27	0.042±0.050	0.045±0.030	0.041±0.030

Table A1. The slope, scatter and tightness for the reduced sample. Column (1): band; Column (2)-Column (4): slopes of the TFrs based on W_{50}^i , V_{max} and V_{flat} , measured in magnitudes; Column (5)-Column(7): scatter of the TFrs based on W_{50}^i , V_{max} and V_{flat} , measured in magnitudes; Column (8)-Column (10): tightness of the TFrs based on W_{50}^i , V_{max} and V_{flat} , measured in dex;

Band	Slope (Mag)			Scatter (Mag)			Tightness σ_{\perp} (dex)		
	W_{50}^i	V_{max}	V_{flat}	W_{50}^i	V_{max}	V_{flat}	W_{50}^i	V_{max}	V_{flat}
FUV	-7.63±1.73	-7.33±1.74	-8.39±2.20	1.13±0.40	1.10±0.40	1.21±0.44	0.143 ± 0.122	0.144 ± 0.061	0.140 ± 0.061
NUV	-6.95±1.04	-6.69±1.10	-7.46±1.38	0.90±0.31	0.87±0.32	0.93±0.35	0.125 ± 0.079	0.125 ± 0.039	0.121 ± 0.039
u	-7.82±1.38	-7.95±1.11	-8.76±1.27	0.69±0.43	0.65±0.39	0.62±0.41	0.087 ± 0.138	0.082 ± 0.069	0.071 ± 0.069
g	-7.17±0.55	-7.38±0.47	-8.21±0.54	0.32±0.27	0.32±0.25	0.31±0.27	0.044 ± 0.055	0.043 ± 0.027	0.038 ± 0.027
r	-7.76±0.46	-8.01±0.42	-8.92±0.51	0.28±0.25	0.29±0.24	0.28±0.26	0.046 ± 0.046	0.046 ± 0.023	0.042 ± 0.023
i	-8.15±0.54	-8.38±0.47	-9.36±0.59	0.31±0.27	0.30±0.25	0.30±0.28	0.048 ± 0.055	0.046 ± 0.027	0.039 ± 0.027
z	-8.58±0.69	-8.81±0.60	-9.85±0.74	0.37±0.31	0.34±0.28	0.36±0.32	0.045 ± 0.086	0.043 ± 0.043	0.042 ± 0.043
J	-8.93±0.51	-9.12±0.57	-9.97±0.67	0.38±0.22	0.43±0.23	0.43±0.25	0.048 ± 0.042	0.047 ± 0.021	0.044 ± 0.021
H	-8.99±0.56	-9.22±0.67	-9.99±0.61	0.39±0.23	0.46±0.26	0.41±0.24	0.046 ± 0.071	0.051 ± 0.035	0.044 ± 0.035
K	-9.38±0.54	-9.61±0.63	-10.46±0.68	0.41±0.22	0.47±0.25	0.45±0.25	0.044 ± 0.045	0.049 ± 0.023	0.043 ± 0.023
3.6	-9.56±0.46	-9.37±0.42	-10.08±0.40	0.42±0.20	0.44±0.19	0.38±0.19	0.043 ± 0.038	0.046 ± 0.019	0.037 ± 0.019
4.5	-9.65±0.53	-9.44±0.43	-10.16±0.41	0.45±0.21	0.46±0.20	0.40±0.19	0.047 ± 0.044	0.048 ± 0.022	0.040 ± 0.022

Table B1. The slope, scatter and tightness for the TFrs, based on 2.2h magnitudes Column (1): band; Column (2)-Column (4): slopes of the TFrs based on W_{50}^i , V_{max} and V_{flat} , measured in magnitudes; Column (5)-Column(7): scatter of the TFrs based on W_{50}^i , V_{max} and V_{flat} , measured in magnitudes; Column (8)-Column (10): tightness of the TFrs based on W_{50}^i , V_{max} and V_{flat} , measured in dex;

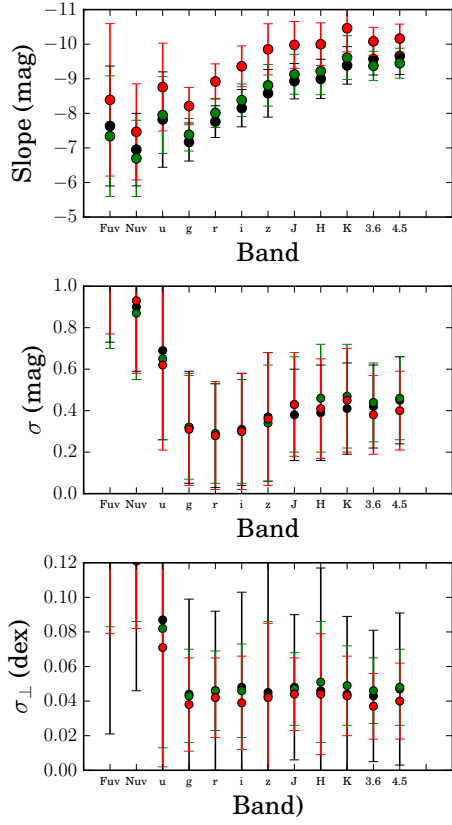


Figure B1. Slope, scatter and tightness of the TFR based on magnitudes measured at $2.2h$, as a function of wavelength, calculated using different rotation measures. With black points indicated values measured for the TFR based on W_{50}^i , with green based on V_{max} and with red based on V_{flat} .